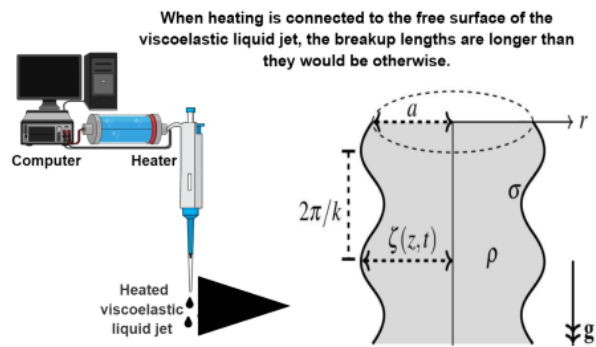


7406B31229D5403B9A04D972B19CCD3
C

Graphical Abstract

Thermocapillary effects on absolute and convective instability of viscoelastic liquid jets

A. Alhushaybari



Highlights

24

Thermocapillary effects on absolute and convective instability of viscoelastic liquid jets

A. Alhushaybari

- The viscoelastic liquid jet's tendency to disintegrate is slowed down by heating, which has a stabilizing effect.
- When heat transfer to the interface of the viscoelastic liquid jet is considered, a dripping-to-jetting transition occurs at lower values of the critical Weber number.
- When heating is connected to the free surface of the viscoelastic jet, the breakup lengths are longer than they would be otherwise.

Thermocapillary effects on absolute and convective instability of viscoelastic liquid jets

A. Alhushaybari^a

^a*Department of Mathematics, College of Science, Taif University, Taif, P.O. Box 11099, Taif 21944, Saudi Arabia*

Abstract

The effect of heat transmission on the absolute instability (AI) and convective instability (CI) of axisymmetrical disturbances in a viscoelastic liquid jet that falls under gravity is investigated. In general, when heat is included to the interface of a viscoelastic jet, it can be used to process droplet sizes and breakup lengths even more. We describe the jet's dynamics mathematically using the Upper-Convected Maxwell (UCM) model. On the basis of the jet's slenderness, an asymptotic approach is used to simplify the problem and obtain solutions of steady basic flow, which are then linearly analyzed for absolute and convective instability. When traveling wave modes are considered, a dispersion relation between the wavenumber and the growth rate of viscoelastic jets is derived, which can then be solved numerically using the Newton-Raphson method. The impact of varying some non-dimensional parameters is shown on absolute and convective instability. In this work, absolute instability is explored by employing a mapping technique called the cusp map method. For a variety of parameter regimes, the convective-to-absolute instability boundary (CAIB) is determined. We have found that absolute-to-convective transitions occur at lower critical Weber numbers when heating is included to the interface of the viscoelastic jets.

Keywords: Viscoelastic Liquid Jets, Absolute Instability, Heat Transfer, Cusp Map Method

1. Introduction

In liquid jets, the role of capillary thermodynamic effects on the (CI) and (AI) are still an open area of research and not well understood completely. (Bauer, 1984) was the first to examine the instability of non-isothermal jets (with temperature-dependent surface tension) by using linear stability theory. (Bauer, 1984) looked

specifically at the case of the Stokes flow with adding temperature to the jet surface. He found that the jet can be broken up because of oscillating temperature gradients along the jet interface. (Xu and Davis, 1985) studied especially the linear axial distribution of temperature along the jet surface. They found that the capillary instability can be repressed, or obstructed by the instability of the surface wave produced by surface tension gradients. Whereas the first work in controlling the liquid jet disintegration was carried out by (Faidley and Panton, 1990) using a quick-response nozzle heater to control surface tension. They found that the Rayleigh mode was dominant and that the thermal effects were unimportant to the growth of the disturbances. However, by using a CO_2 laser beam with sufficient intensity, (Nahas and Panton, 1990) were able to demonstrate that it could be eliminated the initial turbulence on the jet surface, which indicates that the heater utilized by (Faidley and Panton, 1990) was not able to generate adequate nozzle heating.

The instability and following disintegration of the liquid jet column is important in a variety of emerging applications (for example, needleless injection (see Moradiafrapoli and Marston, 2017), nanofiber (see Gadkari, 2017), ink-jet printing (see Du et al., 2018), coating, and even technology of diesel engine (see Eggers and Villermaux, 2008). Although more than 200 years passed of scientific scrutiny, liquid jet instability is still an interesting area of study for many researchers in various scientific fields. A liquid jet may be defined as a stream that can be injected into a medium of liquid or gas through an opening (a nozzle). Liquid jets, in general, are naturally unstable and eventually disintegrated into drops. The Rayleigh-Plateau instability is the main mechanism of this dissociation and determined by the growth of perturbations that are either convective or absolute instability. Convective instability can be growing in amplitude when it is swept along by the liquid flow, while absolute instability can occur at particular spatial positions (see Bassi, 2011). Moreover, the formation of the droplet occurs either directly at the jet's outlet or downstream, at the flow's end. Jetting and dripping are the terms used to describe these two instabilities respectively (see Suñol and González-Cinca, 2015).

The first investigation of absolute instability related to liquid jets was done by (Leib and Goldstein, 1986b). They revealed that the capillary absolute instability of an inviscid jet is generated at small Weber numbers because of surface tension. They identified critical Weber numbers (We) that indicate the transition from (CI) to (AI). They showed that when the Weber number is less than 3.15, the inviscid liquid jet is absolutely unstable; whereas it is convectively unstable when $We > 3.15$. (Leib and Goldstein, 1986a) examined the viscosity effect on

the transition from (CI) to (AI) and found a decrease in values of critical Weber number when We is a function of Re (where Re is the Reynolds number). Using the $Re - We$ plane, they plotted the relationship between Re and We numbers and discovered a crucial curve that distinguishes the area between absolute and convective instability. A criterion for analyzing absolute instability developed by (Briggs, 1964) was used by (Lin and Lian, 1989) to find the transition boundary between (CI) and (AI) for a viscous liquid in the presence of a surrounding gas. (Alhushaybari and Uddin, 2019) investigated the (CI) and (AI) of a viscoelastic liquid jet falling vertically due to gravity. They showed the convective/absolute instability boundaries (CAIB) in different parameter regimes and especially compared the (CAIB) in the $Re - We$ plane with other authors investigated the viscous case such as (Lin and Lian, 1989, 1993), (Leib and Goldstein, 1986a) and (López-Herrera et al., 2010).

Nowadays, the instability for a liquid jet having complex rheology is significant in various emerging and growing applications (such as needle-free injections and fiber spinning where the jet stability is a prerequisite for the formation of fibers with desirable properties or successful injection (i.e. skin breakthrough) (see Moradiafrapoli and Marston, 2017). The instability of viscoelastic liquid jets also has some important applications in geodynamic fields related to underground mechanical explosions and earthquakes (see (Sharma et al., 2020), (Pramanik and Manna, 2022) and (Manna et al., 2018)). In these and other applications, the fluid utilized predominate contains additional quantities or biological agents that lead to the appearance of viscoelastic properties, and where instability is not desirable and the use of heating provides a technique for reducing the growth rates of unstable waves along the interface. In these applications, the use of heating provides one mechanism by which the growth of instability can be delayed. In light of this, this article investigates the absolute instability of a viscoelastic jet that is heated at the nozzle and falls under gravity. We employ a mapping technique dubbed the 'Cusp Map Method' developed by (Kupfer et al., 1987) to locate the cusp point corresponding to the pinch point, which indicates the transition of convective-to-absolute instability.

2. Problem Formulation

Consider an axisymmetrical viscoelastic jet has radius a , surface tension σ , thermal conductivity k_t , temperature H , density ρ , heat capacity C_p and mean velocity U , which emerges from a nozzle, and falls under gravity into a surrounding of an inviscid gas, which has lower temperature H_a and density ρ_a . The jet

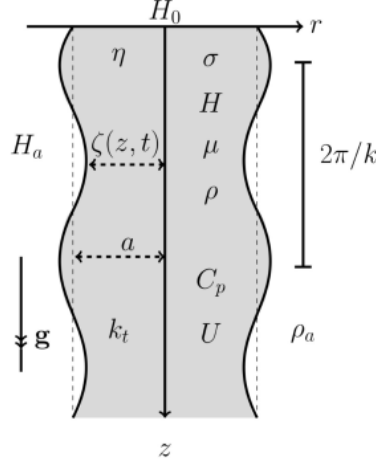


Figure 1: A diagram of a viscoelastic liquid jet emerging from a nozzle with computer-controlled heating.

leaving the nozzle is heated by a heater, which is connected to a computer so that the heating can be done in a controlled manner with a convenient frequency. To consider the axial symmetry problem, we suppose that the jet cross-section remains circular ($\frac{\partial}{\partial \theta} = 0$), and no swirl occurs ($v_\theta = 0$), so the velocity vector is $\mathbf{v} = (v_r, 0, v_z)$. The boundary conditions, as well as the governing equations, will be written in a cylindrical coordinate system where the z -axis runs parallel axis to the direction of the flow, whereas the r -axis runs perpendicular to the z -axis as depicted in Fig. 1.

In viscoelastic fluids, the relation between stress and strain can be expressed by the Upper-Convected Maxwell model (see Bird et al., 1987), which is

$$\tau = \mu_p \dot{\eta} - \lambda \tau^\diamond, \quad (1)$$

where μ_p denotes the viscosity of the polymer, τ denotes the extra stress tensor (which brings the elastic effects), $\dot{\eta}$ is the component of the strain-rate tensor that is symmetric and defined by $\dot{\eta} = \nabla \mathbf{v} + (\nabla \mathbf{v})^T$, λ is the relaxation time, and τ^\diamond is defined by

$$\tau^\diamond = \frac{\partial \tau}{\partial t} + (\mathbf{v} \cdot \nabla) \tau - \tau \cdot \nabla \mathbf{v} - (\nabla \mathbf{v})^T \cdot \tau, \quad (2)$$

which stands for the upper-convected time derivative of τ , where t is the time.

Therefore, for an incompressible viscoelastic jet, the continuity equation is

$$\nabla \cdot \mathbf{v} = 0, \quad (3)$$

while the equation of momentum takes the form

$$\left(\frac{\partial}{\partial t} + \mathbf{v} \cdot \nabla \right) \mathbf{v} = \frac{1}{\rho} \left(-\nabla p + \nabla \cdot \mathbf{T} \right) + \mathbf{g}, \quad (4)$$

where

$$\mathbf{T} = \mu \dot{\boldsymbol{\eta}} - \lambda \boldsymbol{\tau}^\diamond, \quad (5)$$

$\mathbf{g} = (0, 0, g)$, p is the pressure, and μ is the overall viscosity of solvent and polymer components at zero-shear. The position of the viscoelastic free-surface may be described as $r = \zeta(z, t)$. Moreover, this position of the free surface must be determined as part of the solution to the flow equations, which are distinct from earlier flow states that established prior boundaries. The relationship between the surface tension, σ , and the jet temperature, H , may be expressed linearly by

$$\sigma = \sigma_a + \sigma_H (H - H_a), \quad (6)$$

where σ_H is a constant coefficient, given by $\left(\frac{d\sigma}{dH} \right)_{H=H_a}$, and σ_a is the surface tension at the ambient temperature H_a . Since the viscosity of a fluid is affected by temperature change, most fluids can be described by the relation of the Arrhenius type (see Chwalek et al., 2002) and (Atencia and Beebe, 2004))

$$\mu = \mu_a + \mu_H (H - H_a), \quad (7)$$

where μ_H is a constant coefficient, given by $\left(\frac{d\mu}{dH} \right)_{H=H_a}$, and μ_a is the liquid viscosity at the ambient temperature. The energy equation is given by

$$\frac{\partial H}{\partial t} + v_r \frac{\partial H}{\partial r} + v_z \frac{\partial H}{\partial z} = \frac{k_t}{\rho C_p} \left(\frac{\partial^2 H}{\partial r^2} + \frac{1}{r} \frac{\partial H}{\partial r} + \frac{\partial^2 H}{\partial z^2} \right). \quad (8)$$

At the jet interface, the boundary conditions are assessed by comparing the pressure across the free surface to the normal stresses, which are linked to the mean curvature by the relationship

$$\mathbf{n} \cdot \boldsymbol{\Omega} \cdot \mathbf{n} = \sigma R \text{ at } r = \zeta, \quad (9)$$

22

where \mathbf{n} is the normal unit vector, Ω denotes the entire stress tensor given by $\Omega = -p\mathbf{I} + \mathbf{T}$, and R is the mean curvature of the viscoelastic liquid surface given by

$$R = \frac{1}{E^3} \left(\frac{E^2}{\zeta} - \frac{\partial^2 \zeta}{\partial z^2} \right), \text{ where } E = \sqrt{1 + \left(\frac{\partial \zeta}{\partial z} \right)^2}.$$

The tangential stresses are balanced by thermocapillary force along the free surface given by

$$\mathbf{t} \cdot \Omega \cdot \mathbf{n} = \mathbf{t} \cdot \nabla \sigma \text{ at } r = \zeta, \quad (10)$$

where \mathbf{t} is the tangential unit vector. The normal flux of heat across the free surface can be described by Newton's law of cooling, which is

$$-k_t(\mathbf{n} \cdot \nabla H) = S(H - H_a) \text{ at } r = \zeta, \quad (11)$$

where S is the coefficient of the thermal transfer that gives the rate of the heat transfer from the viscoelastic jet to its surrounding. The right side of (11) is zero if the free surface is assumed to be thermally insulated. Also, the kinematic boundary condition is required to keep viscoelastic liquid jet particles staying on the jet interface, which is

$$\left(\frac{\partial}{\partial t} + \mathbf{v} \cdot \nabla \right) (r - \zeta) = 0 \text{ at } r = \zeta, \quad (12)$$

3. Dimensionless Analysis

Non-dimensionless scales used to write the dimensionless versions of the governing and boundary equations are (see Anno, 1977)

$$\begin{aligned} z^* &= \frac{z}{L}, \quad r^* = \frac{r}{a}, \quad t^* = \frac{U}{L}t, \quad p^* = \frac{p}{U^2\rho}, \quad \varepsilon = \frac{a}{L}, \quad \{v_r^*, v_z^*\} = \frac{1}{U}\{v_r, v_z\}, \\ \zeta^* &= \frac{\zeta}{a}, \quad \{\tau^*, T^*\} = \frac{L}{U\mu_a}\{\tau, T\}, \quad H^* = \frac{H}{H_a}, \quad \sigma^* = \frac{\sigma}{\sigma_a}, \quad \mu^* = \frac{\mu}{\mu_a}, \end{aligned} \quad (13)$$

where U and L are the exit speed of the viscoelastic jet and the axial length scale respectively. The superscript (*) is dropped for convenience, thus the non-dimension parameters, that allow analyzing the viscoelastic jet's flow dynamics, are

$$F = \frac{U}{\sqrt{ag}}, \quad Pe = \frac{LU\rho C_p}{k_t}, \quad We = \frac{\rho U^2 a}{\sigma_a}, \quad De = \frac{\lambda U}{L}, \quad Bi = \frac{LS}{k_t}, \quad Re = \frac{U\rho a}{\mu_a}, \quad (14)$$

where Re , We , F , De , Bi , and Pe are the Reynolds number, Weber number, Froude number, Deborah number, Biot number, and Peclet number respectively. For typical values of viscoelastic fluids that are obtained from industrial applications (see Bird et al., 1977) and (Verhoef et al., 1999)) where $De \sim 10^{-2} - 10^3$, $Pe \sim 10^{-1} - 10^3$, $\mu \sim 10^{-2} - 10^2$, $Bi \sim 10^{-4} - 10$, $Re \sim 10^{-2} - 10^2$ and $\lambda \sim 10^{-3} - 10$, and for a viscoelastic jet having an initial velocity $U \sim 0.3 - 10 \text{ ms}^{-1}$ and a diameter $a = 10^{-3} \text{ m}$. ³ this analysis, these ranges of parameter values are used. The non-dimensional forms of the governing and boundary equations can be found in Appendix A.

4. Asymptotic Analysis

Following (Eggers, 1997), we give the jet a small aspect ratio ($\varepsilon = a/L \ll 1$) by assuming that it is slender. These dimensionless equations (in Appendix A) are investigated in further details, so v_z , v_r , p and H are expanded in a Taylor series in εr ; and ζ , μ , T_{zz} and T_{rr} are expanded in an asymptotic series in ε . Also, we assume that small disturbances have no effect on the viscoelastic jet column's centerline. Since $\zeta(z)$ ²³anges slowly with respect to z (in the long wave limit), thus the pressure (p), the axial velocity (v_z), and the components of the stress tensor (T_{rr} and T_{zz}) are nearly uniform with respect to r whilst T_{rz} is roughly zero. As a result, a Taylor expansion of r is the appropriate ansatz for analyzing slender viscoelastic jets, which means that we have

$$\{v_z, v_r, p, H\} = \{v_{z0}(z, t), v_{r0}(z, t), p_0(z, t), H_0(z, t)\} + \varepsilon r \{v_{z1}(z, t), v_{r1}(z, t), p_1(z, t), H_1(z, t)\} + O(\varepsilon^2 r^2), \quad (15)$$

$$\{T_{zz}, T_{rr}, \zeta, \sigma, \mu\} = \{T_{zz}^0(z, t), T_{rr}^0(z, t), \zeta_0(z, t), \sigma_0(z, t), \mu_0(z, t)\} + \varepsilon \{\zeta_1(z, t), T_{zz}^1(z, t), T_{rr}^1(z, t), \sigma_1(z, t), \mu_1(z, t)\} + O(\varepsilon^2). \quad (16)$$

To maintain viscoelastic and gravitational terms, we rescale the Reynolds and Froude numbers as follows: $Re = \varepsilon \tilde{Re} = O(1)$ and $\varepsilon F^2 = \tilde{F}^2 = O(1)$ (see Uddin, 2007). We substitute the expressions, (15) and (16), into the dimensionless forms (in Appendix A) and removing the tildes for simplicity, we can write the axial

momentum equation, to $O(\varepsilon)$, as

$$\begin{aligned} \frac{\partial v_{z0}}{\partial t} + v_{z0} \frac{\partial v_{z0}}{\partial z} &= \frac{-1}{We} \frac{\partial}{\partial z} \left(\frac{\sigma_0}{\zeta_0} \right) + \frac{3[1 + \mu_H(H_0 - 1)]}{\zeta_0^2 Re} \left[\frac{\partial}{\partial z} \left(\zeta_0^2 \frac{\partial v_{z0}}{\partial z} \right) \right. \\ &\quad \left. - \zeta_0^2 \mu_H \frac{\partial H_0}{\partial z} \frac{\partial v_{z0}}{\partial z} \right] - \frac{2\sigma_H}{\zeta_0 We} \frac{\partial H_0}{\partial z} + \frac{1}{\zeta_0^2 Re} \frac{\partial}{\partial z} \left(\zeta_0^2 (T_{zz}^0 - T_{rr}^0) \right) + \frac{1}{F^2}, \end{aligned} \quad (17)$$

where

$$\sigma_0 = 1 + \sigma_H(H_0 - 1).$$

See more details of the derivation of the equation, (17), in Appendix B. Also, we obtain the components of the extra stress tensor, (A.5) and (A.6), to leading order, which are respectively

$$De \left(\frac{\partial T_{zz}^0}{\partial t} + v_{z0} \frac{\partial T_{zz}^0}{\partial z} - 2T_{zz}^0 \frac{\partial v_{z0}}{\partial z} \right) = 2[1 + \mu_H(H_0 - 1)] \frac{\partial v_{z0}}{\partial z} - T_{zz}^0, \quad (18)$$

$$De \left(\frac{\partial T_{rr}^0}{\partial t} + v_{z0} \frac{\partial T_{rr}^0}{\partial z} + T_{rr}^0 \frac{\partial v_{z0}}{\partial z} \right) = -[1 + \mu_H(H_0 - 1)] \frac{\partial v_{z0}}{\partial z} + T_{rr}^0. \quad (19)$$

If $F \rightarrow \infty$, $\mu_H = \sigma_H = 0$, the last set of equations, (17)-(19), are the same as those obtained by (Clasen et al., 2006, Alhushaybari and Uddin, 2019). From the energy equation (A.7), to $O(1)$ and $O(\varepsilon)$, we have respectively

$$H_1 = 0, \quad (20)$$

and

$$\frac{\partial H_0}{\partial t} + v_{z0} \frac{\partial H_0}{\partial z} = \frac{1}{Pe} \left(4H_2 + \frac{\partial^2 H_0}{\partial z^2} \right). \quad (21)$$

From the boundary conditions, the condition of the normal heat flux (A.10) to leading order becomes

$$H_2 = \frac{1}{2\zeta_0} \frac{\partial \zeta_0}{\partial z} \frac{\partial H_0}{\partial z} - \frac{Bi}{2\zeta_0} (H_0 - 1).$$

Assuming there is low heat transfer to the surrounding environment (as in most liquids when there is a slight temperature difference with the ambient), we have

already re-scaled the Biot number in the previous equation, so that ($\tilde{Bi} = \epsilon Bi = O(1)$). Dropping the tildes for convenience and substituting of H_2 into (21) give

$$\frac{\partial H_0}{\partial t} + v_{z0} \frac{\partial H_0}{\partial z} = \frac{1}{Pe \zeta_0^2} \left(\frac{\partial}{\partial z} \left(\zeta_0^2 \frac{\partial H_0}{\partial z} \right) - 2\tilde{Bi} \zeta_0 (H_0 - 1) \right). \quad (22)$$

The kinematic boundary condition, (A.11), can be written, to leading order, as

$$\frac{\partial (\zeta_0^2 v_{z0})}{\partial z} + \frac{\partial \zeta_0^2}{\partial t} = 0 \quad (23)$$

If $\mu_H = 0$ and $\sigma_H = 0$ (i.e, no changing in viscosity or in surface tension with temperature) and $F \rightarrow \infty$, the last set of equations, (17), (22) and (23), are the same as those obtained by (Furlani, 2005).

5. Solutions of steady basic flow

In order to find steady basic flow solutions of (17)-(23), we first remove all time derivatives and then solve a nonlinear equations system, which has the four variables T_{rr}^0 , v_{z0} , T_{zz}^0 and H_0 as functions of z . Also, we find from (23) that $v_{z0} \zeta_0^2$ is constant, and using the boundary conditions at the nozzle ($v_{z0}(0) = 1$ and $\zeta_0(0) = 1$) lead to have that $v_{z0} \zeta_0^2 = 1$, and consequently the equations (17)-(19) and (22) become respectively

$$\begin{aligned} v_{z0} \frac{\partial v_{z0}}{\partial z} = & \frac{-1}{We} \left(\frac{1 - \sigma_H(H_0 - 1)}{2\sqrt{v_{z0}}} \frac{\partial v_{z0}}{\partial z} - \sqrt{v_{z0}} \sigma_H \frac{\partial H_0}{\partial z} \right) \\ & + \frac{3(1 + \mu_H(H_0 - 1))}{Re} \left(\frac{\partial^2 v_{z0}}{\partial z^2} - \frac{1}{v_{z0}} \left(\frac{\partial v_{z0}}{\partial z} \right)^2 - \mu_H \frac{\partial H_0}{\partial z} \frac{\partial v_{z0}}{\partial z} \right) \\ & + \frac{1}{Re} \left(\frac{\partial}{\partial z} (T_{zz}^0 - T_{rr}^0) - \frac{1}{v_{z0}} \frac{\partial v_{z0}}{\partial z} (T_{zz}^0 - T_{rr}^0) \right) - \frac{2\sigma_H \sqrt{v_{z0}}}{We} \frac{\partial H_0}{\partial z} + \frac{1}{F^2}, \quad (24) \end{aligned}$$

$$De \left(v_{z0} \frac{\partial T_{zz}^0}{\partial z} - 2T_{zz}^0 \frac{\partial v_{z0}}{\partial z} \right) = 2[1 + \mu_H(H_0 - 1)] \frac{\partial v_{z0}}{\partial z} - T_{zz}^0, \quad (25)$$

$$De \left(v_{z0} \frac{\partial T_{rr}^0}{\partial z} + T_{rr}^0 \frac{\partial v_{z0}}{\partial z} \right) = -[1 + \mu_H(H_0 - 1)] \frac{\partial v_{z0}}{\partial z} + T_{rr}^0, \quad (26)$$

and

$$v_{z0} \frac{\partial H_0}{\partial z} = \frac{1}{Pe} \left(\frac{\partial^2 H_0}{\partial z^2} - \frac{1}{v_{z0}} \frac{\partial H_0}{\partial z} \frac{\partial v_{z0}}{\partial z} - 2Bi \sqrt{v_{z0}} (H_0 - 1) \right). \quad (27)$$

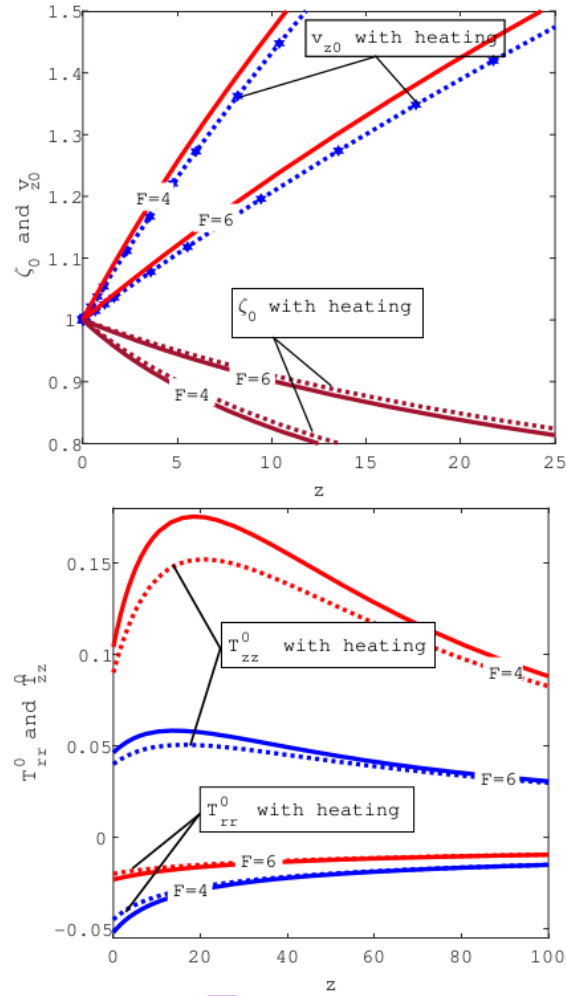
The nonlinear system of ordinary differential equations, (24)-(27), are solved using the Runge-Kutta method (found in MATLAB (*ode45*)). Fig. 2 shows the gravity effect (through Froude's different numbers F) on steady basic flow solutions (T_{rr}^0 , T_{zz}^0 , ζ_0 , v_{z0} and H_0) against the axial length of the jet (z) with and without heating. Solid lines show the solutions of the steady basic flow without heating; while dotted lines are the corresponding solutions with heating. We can see, from this figure, that a reduction in F accelerates the jet's thinning and axial velocity increases. The inclusion of heating leads to an increase in the steady velocity along the viscoelastic jet leading to a faster decay in the radius of the jet along the z -direction of the jet. This is a consequence of the fact that the initial heating value H_0 decreases along the jet (see Fig.3) and, as a result, the surface tension increases with distance from the nozzle (the surface tension does, in fact, increase monotonically along the viscoelastic jet). We can see from Fig. 2 that this variation in surface tension causes a Marangoni flow to be induced along the jet axis. Because this flow operates in the direction of rising surface tension, the jet will accelerate toward the direction of gravity as a result. We conclude, from this result, that the heat energy transfer along the jet causes a Marangoni-type flow, that helps to make the jet thinner, leading to shorter lengths of breakup. We also can be seen that the steady axial tensor (T_{zz}^0) of the viscoelastic liquid jet decreases with heating along the flow direction, whilst the steady radial tensor (T_{rr}^0) increases. Moreover, we can also notice that increasing F leads to a decrease in (T_{zz}^0) and an increase in (T_{rr}^0) along the flow direction.

6. Analysis of Linear Instability

Over an axial length scale of $z = O(1)$, the viscoelastic jet develops. But, waves (having wavelengths of $O(a)$) are much smaller along the viscoelastic jet, that are analogous to ε in a scenario where $z = O(\varepsilon)$ is present. This multiscale technique was utilized by (Uddin, 2007). We use $\exp(ik\bar{z} + \omega\bar{t})$ as a model for the traveling wave mode, where $t = \varepsilon\bar{t}$, $z = \varepsilon\bar{z}$, $k = k(z) = O(1)$ and $\omega = \omega(z) = O(1)$. We use the following substitutions to apply a small perturbation about the solutions of the steady basic flow, which are

$$\left\{ v_z, v_r, \zeta, T_{zz}, T_{rr}, p, \sigma, H \right\} = \left\{ v_{z0}(z), 0, \zeta_0(z), T_{zz}^0(z), T_{rr}^0(z), p_0(z), \sigma_0(z), H_0(z) \right\} + \delta \left\{ \tilde{v}_z(r), \tilde{v}_r(r), \tilde{\zeta}, \tilde{T}_{zz}(r), \tilde{T}_{rr}(r), \tilde{p}(r), \tilde{\sigma}(r), \tilde{H}(r) \right\} \times \exp(ik(z)\bar{z} + \omega(z)\bar{t}), \quad (28)$$

These expressions are substituted into our non-dimensional forms (in Appendix A) with keeping only $O(\delta)$ terms, and after removing the tilde signs for simplicity,



27

Figure 2: v_{z0} , ζ_0 , T_{zz}^0 and T_{rr}^0 are plotted as a function of z for various values of F , where the solid lines show the steady basic solutions without heating (published by (Alhushaybari and Uddin, 2019)) with $\mu_H = H_0 = \sigma_H = 0$, and the dotted lines show the steady basic solutions with heating (current work with $\mu_H = 0.2$, $H_0 = 2$ and $\sigma_H = 0.1$). Where $De = 10$, $Re = 800$, $Pe = 10$, $Bi = 0.2$ and $We = 2$.

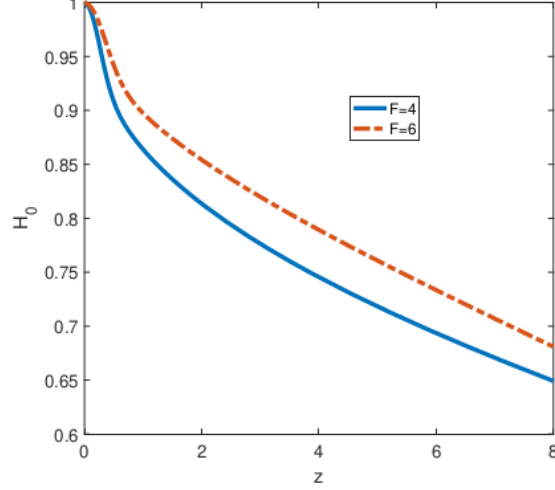


Figure 3: H_0 is plotted as a function of z with various values of F . Where $Re = 800$, $De = 10$, $Pe = 10$, $Bi = 0.2$, $We = 2$, $\mu_H = 0.2$ and $\sigma_H = 0.1$.

we arrive at an ODE system of equations (see Appendix C). Therefore, solving this system and utilizing the boundary conditions give the forms of the pressure profile, and the radial and axial velocity profiles, which are respectively

$$\bar{p} = - \left\{ \frac{I_0(hr)}{I_1(h\xi_0)} \left(\frac{[1 + \mu_H(H_0 - 1)](1 + c)\Lambda + c(T_{rr}^0 - T_{zz}^0)}{(ch^2 - k^2)} \right) \times \right. \\ \left. \frac{2hk^2(T_{rr}^0 + \frac{1 + \mu_H(H_0 - 1)}{De})}{Re\Lambda} + \left(\frac{\Lambda}{k^2} + \frac{2(T_{zz}^0 + \frac{1 + \mu_H(H_0 - 1)}{De})}{Re\Lambda} \right) \times \right. \\ \left. \left(\frac{\sqrt{ck} \left([1 + \mu_H(H_0 - 1)](h^2 + k^2)\Lambda + k^2(T_{rr}^0 - T_{zz}^0) \right)}{(ch^2 - k^2)} \right) \frac{I_0(kr/\sqrt{c})}{I_1(k\xi_0/\sqrt{c})} \right\} \bar{\xi}, \quad (29)$$

$$\bar{v}_r = \left\{ \left(\frac{c[1 + \mu_H(H_0 - 1)](h^2 + k^2)\Lambda + ck^2(T_{rr}^0 - T_{zz}^0)}{(ch^2 - k^2)} \right) \frac{I_1(kr/\sqrt{c})}{I_1(k\xi_0/\sqrt{c})} \right. \\ \left. - \left[\frac{[1 + \mu_H(H_0 - 1)](1 + c)k^2\Lambda + ck^2(T_{rr}^0 - T_{zz}^0)}{(ch^2 - k^2)} \right] \frac{I_1(hr)}{I_1(h\xi_0)} \right\} \bar{\xi}, \quad (30)$$

$$\bar{v}_z = i \left\{ \frac{\sqrt{c}[1 + \mu_H(H_0 - 1)](h^2 + k^2)\Lambda + \sqrt{c}k^2(T_{rr}^0 - T_{zz}^0)}{(ch^2 - k^2)} \frac{I_0(kr/\sqrt{c})}{I_1(k\zeta_0/\sqrt{c})} - \frac{[1 + \mu_H(H_0 - 1)](1 + c)kh\Lambda + ckh(T_{rr}^0 - T_{zz}^0)}{(ch^2 - k^2)} \frac{I_0(hr)}{I_1(h\zeta_0)} \right\} \bar{\xi}, \quad (31)$$

where

$$c = \left\{ [1 + \mu_H(H_0 - 1)]\Lambda(D_0 - h^2) \right\} / \left\{ 2k^2 \left(T_{rr}^0 + T_{zz}^0 + \frac{2 - 2\mu_H(H_0 - 1)}{De} \right) + [1 + \mu_H(H_0 - 1)]\Lambda(D_0 - h^2) + \frac{2}{r^2} \left(T_{rr}^0 + \frac{1 + \mu_H(H_0 - 1)}{De} \right) \right\},$$

$$h^2 = k^2 + \frac{\Lambda}{[1 + \mu_H(H_0 - 1)]} \left\{ Re + \frac{2k^2}{\Lambda^2} \left(T_{zz}^0 + T_{rr}^0 + \frac{2 - 2\mu_H(H_0 - 1)}{De} \right) \right\},$$

where I_1 and K_1 are the 1st and 2nd kind of the 1st order modified Bessel function respectively, and $\Lambda = \omega + ikv_{z0}$. Substituting these solutions (29)-(31) into the boundary condition, (C.7) give the dispersion relation

$$\begin{aligned} & \Lambda^2 + \frac{2k^2}{Re} \left[T_{zz}^0 + \frac{1 + \mu_H(H_0 - 1)}{De} \right] + \frac{2k^2}{Re} \frac{I_1'(k\zeta_0/\sqrt{c})}{I_0(k\zeta_0/\sqrt{c})} \left[[1 + \mu_H(H_0 - 1)]\Lambda \right. \\ & \left. + \left(T_{rr}^0 + \frac{1 + \mu_H(H_0 - 1)}{De} \right) \right] + \frac{2hk^3}{Re} \left[\frac{[1 + \mu_H(H_0 - 1)](1 + c)\Lambda + c(T_{rr}^0 - T_{zz}^0)}{\sqrt{c}((h^2 + k^2)\Lambda + k^2(T_{rr}^0 - T_{zz}^0))} \right] \times \\ & \frac{I_1(k\zeta_0/\sqrt{c})}{I_0(k\zeta_0/\sqrt{c})} \left[\left(T_{rr}^0 + \frac{1 + \mu_H(H_0 - 1)}{De} \right) \left(\frac{I_0(h\zeta_0)}{I_1(h\zeta_0)} - \frac{I_1'(h\zeta_0)}{I_1(h\zeta_0)} \right) - \Lambda(1 + \mu_H(H_0 - 1)) \right. \\ & \left. \times \frac{I_1'(h\zeta_0)}{I_1(h\zeta_0)} \right] = \left(\frac{\Lambda k [1 + \mu_H(H_0 - 1)] (ch^2 - k^2) (1 - k^2 \zeta_0^2)}{\sqrt{c} (\Lambda(h^2 + k^2) + k^2(T_{rr}^0 - T_{zz}^0)) We \zeta_0^2} \right) \frac{I_1(k\zeta_0/\sqrt{c})}{I_0(k\zeta_0/\sqrt{c})}. \quad (32) \end{aligned}$$

7. Convective Instability Analysis

The convective instability analysis includes two different instability analyses: temporal instability analysis, where it requires real wavenumber and complex frequency, and spatial instability analysis, where it requires the wavenumber to be complex and the frequency to be purely imaginary.

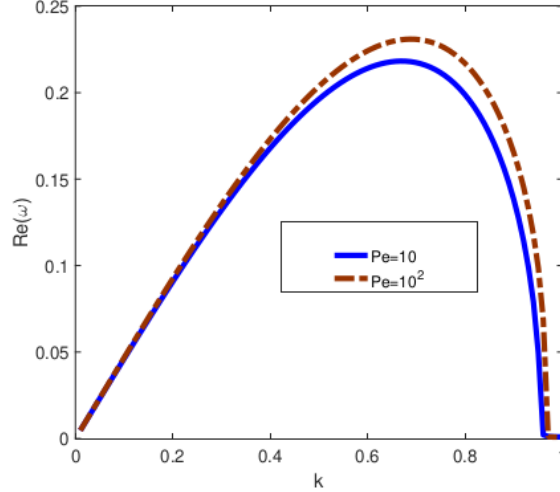


Figure 4: ω_r against k for two different Peclet numbers. Where $F = 4$, $Re = 800$, $Bi = 0.2$, $De = 10$, $\mu_H = 0.2$ and $\sigma_H = 0.1$ at $z = 0$.

7.1. Temporal instability analysis

In the dispersion relation, (32), we consider k as a real wavenumber and ω as a complex frequency, where ω_i is 2π times frequency of the perturbation and ω_r is the perturbation growth rate. Then the Newton-Raphson method is utilized to solve this relation. Solving this dispersion relation yields the wavenumber corresponding to the greatest value of $Re(\omega)$, which is the highest unstable wavenumber. The values of the steady basic flow vary with z , so the related wavenumber will also vary (see section 5), therefore the corresponding growth rate will also change downstream (see Uddin, 2007).

The relation between $Re(\omega)$ and k is plotted, for two different Peclet numbers, as depicted in Fig. 4. From this figure, we see that when the Peclet number is decreased (which corresponds to a stronger influence of thermal diffusion over inertia), the growth rate drops and jets become longer. Also we can see that the highest unstable wavenumber is increased by increasing the Peclet number. The highest unstable wavenumber can be thought of as an inverse standard (by wavelengths) of the expected droplet sizes. In this consideration, Fig. 4 indicates that increasing the Peclet number will result in shorter jets as well as reduced droplet sizes. In Fig. 5 the temporal growth rate for various values of the Biot number is plotted. We note, from this figure, that the growth rate decreases as the Biot

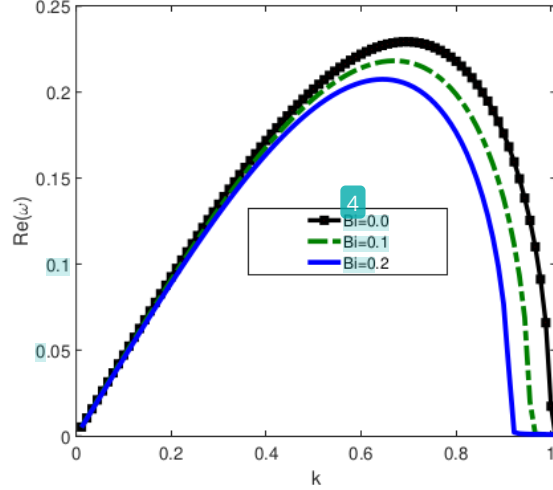
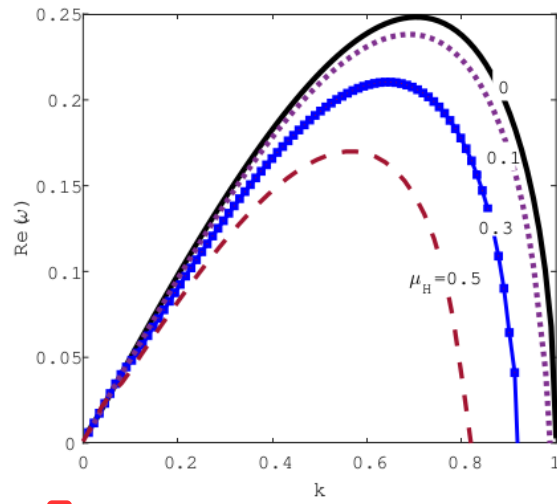


Figure 5: ω_r against k for different Biot numbers. Where $F = 4$, $Re = 800$, $Pe = 10$, $We = 2$, $\mu_H = 0.2$ and $\sigma_H = 0.1$ at $z = 0$.

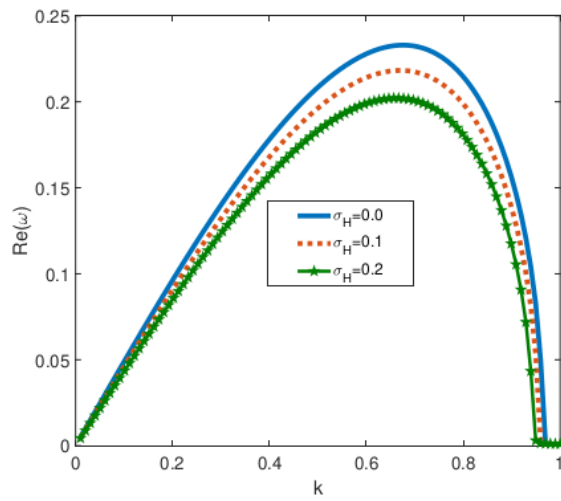
number increases. Also, we plot the relation between $Re(\omega)$ and k , for four different values of μ_H , as depicted in Fig. 6. As illustrated in this figure, the growth rate decreases as the value of μ_H increases. Additionally, we plot the relationship between $Re(\omega)$ and k for various values of σ_H in Fig. 7. We find that increasing the value of σ_H results in a decrease in the growth rate, as illustrated in this figure. Thus we might expect that viscoelastic jets will be longer with heating (because of the reduced growth rate of the perturbation) with larger drops (because of greater wavelengths corresponding to the faster-growing mode). Furthermore, from Fig. 5, we note that an increase in the Biot number reduces the range of instability (that is, the range of k values that causes growth in the waves). These results are in line with observations by (Uddin, 2007) for viscous liquid jets with heating.

7.2. Spatial instability analysis

A spatial instability analysis proposed by (Keller et al., 1973) is a more physically realistic analysis of the investigation of a liquid jet instability spatially, where disturbances grow in space rather than with time. This analysis assumed to set k as a complex wavenumber and ω as an imaginary frequency. Therefore, the spatial instability may be better in describing the physical process of the jet disintegration (see Busker et al., 1989). Spatial instability is also used in simulating satellites that form before or after the formation of the main droplets based on the amplitude of



1
 Figure 6: ω_r against k for different values of μ_H . Where $F = 4$, $Re = 800$, $Pe = 10$, $We = 2$, $Bi = 0.2$ and $\sigma_H = 0.1$ at $z = 0$.



1
 Figure 7: ω_r against k for different values of σ_H . Where $F = 4$, $Re = 800$, $Pe = 10$, $We = 2$, $Bi = 0.2$ and $\mu_H = 0.2$ at $z = 0$.

the disturbance. Comparison of theoretical foretelling and experimental findings carried out by (Si et al., 2009) points out that spatial instability results are in line with experiments better than temporal instability analysis, especially for medium to large Weber numbers (see Xie et al., 2017).

Following (Keller et al., 1973), in the dispersion relation (32), we consider k as a complex wavenumber and ω as a real frequency, where $Im(k)$ is the spatial perturbation growth rate. For unstable perturbations, we need $Im(k) < 0$ since the most negative value of $Im(k)$ gives the largest spatial growth rate. We use the numerical method of Newton-Raphson to solve this dispersion relation for k together with given values of ω . We plot the relation between $Re(k)$ and $Im(k)$ for different values of Pe and Bi as depicted in Fig. 8 and Fig. 9 respectively. We notice from Fig. 8 that the spatial growth rate is decreased when the Peclet number is decreased. While we notice from Fig. 9 that the spatial growth rate is decreased by increasing the values of the Biot number, which means that connecting heating to the free surface of the viscoelastic jet results in longer breakup lengths (i.e. heating has a stabilizing effect on the disintegration of the viscoelastic jet). Also, we observe from Fig. 8 and Fig. 9 that the range of instability (i.e., values of k_r at which the viscoelastic jet is unstable) is affected, where the inclusion of heating leads to a reduction in this range of instability. Also, we plot the relation between $Re(\omega)$ and $Im(\omega)$, for three different values of σ_H , as depicted in Fig. 10. As illustrated in this figure, the spatial growth rate decreases as the value of σ_H decreases. Additionally, we plot the relationship between $Re(\omega)$ and $Im(\omega)$ for various values of μ_H in Fig. 11. We find that increasing the value of μ_H results in a decrease in the spatial growth rate, as illustrated in this figure.

8. Absolute Instability Analysis

Depending on the wave packets' movement that growing along the viscoelastic jet, there are two different kinds of instability. We say that the flow is absolute instability when entire wave packets move up or down and there are time-dependent perturbations that grow at every fixed spatial point. If not, the flow could be convective instability, which grows and spreads far from its point of origin. This gives rise to the viscoelastic jet rupturing elsewhere away from the origin and leaving the jet to be unaffected at this origin (see Drazin and Reid, 1981). In turn, absolute instability spreads far from its origin point; however, it destabilizes the viscoelastic jet everywhere, including at the point of origin of the disturbance. For absolute instability, following (Briggs, 1964) criterion, we take a wave mode $exp(\omega t + ikz)$, where ω and k are both complex. Therefore, absolute instability

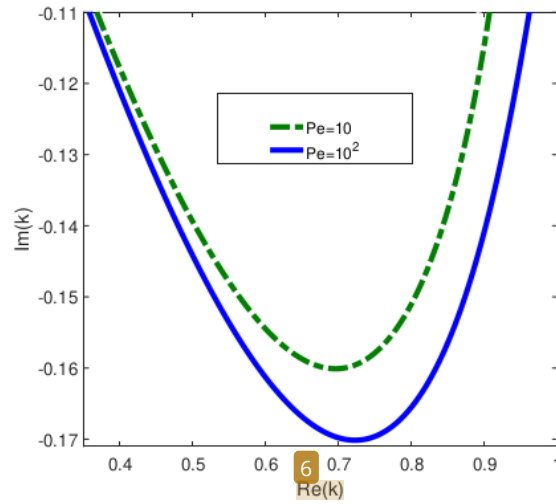


Figure 8: The graph illustrates the relationship between $Im(k)$ and $Re(k)$ for various Peclet numbers. Where $De = 10$, $We = 2$, $F = 4$, $Bi = 0.2$, $\mu_H = 0.2$, $Re = 800$ and $\sigma_H = 0.1$ at $z = 0$.

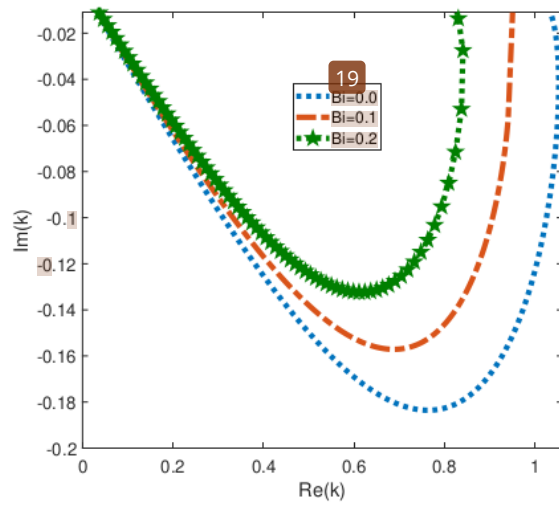
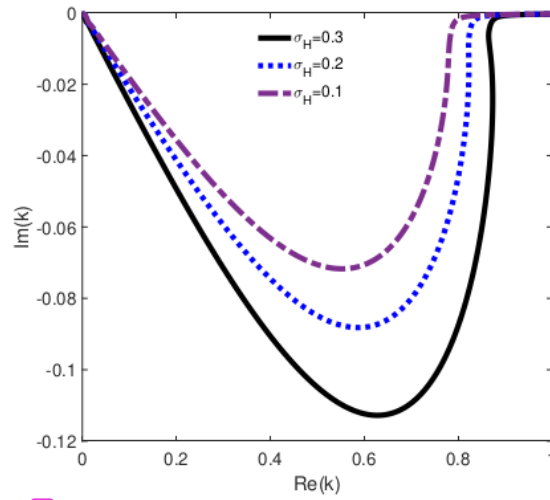
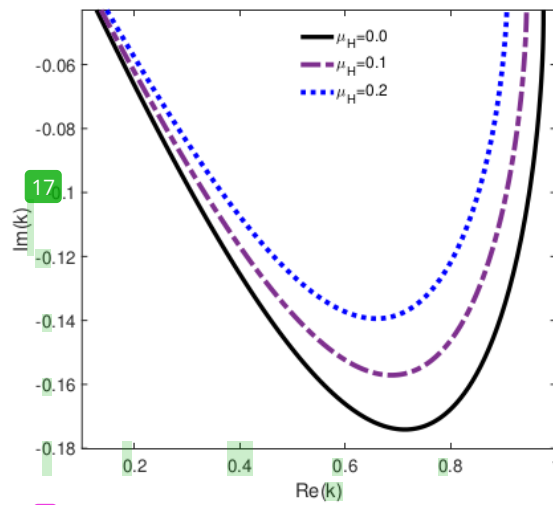


Figure 9: Graph of the spatial growth rate versus the wavenumber for various Biot numbers. Where $We = 2$, $De = 10$, $\mu_H = 0.2$, $Pe = 10$, $\sigma_H = 0.1$, $F = 4$ and $Re = 800$ at $z = 0$.



2
 Figure 10: Graph of the spatial growth rate versus the wavenumber for various values of σ_H . Where $We = 2$, $De = 10$, $\mu_H = 0.2$, $Pe = 10$, $Bi = 0.2$, $F = 4$ and $Re = 800$ at $z = 0$.



17
 2
 Figure 11: Graph of the spatial growth rate versus the wavenumber for various values of μ_H . Where $We = 2$, $De = 10$, $\sigma_H = 0.1$, $Pe = 10$, $Bi = 0.2$, $F = 4$ and $Re = 800$ at $z = 0$.

takes place if the solution of (32) is found in the complex k -plane. This solution is called a saddle point corresponding to a cusp point (a pinch point) in the complex ω -plane.

When two $k(\omega)$ curves in the complex-frequency plane intersect, it forms a “cusp point”. Absolute instability necessitates a $Re(\omega) > 0$ dispersion relation solution. Confirmation of absolute instability occurs when the group velocity (given by a $\partial\omega/\partial k$) is 0 at the k_0 saddle point (which is a necessary condition, but not a sufficient one). This is due to the fact that the group velocity is not just zero in saddle points, but also at the convergence of two k branches regardless of whether or not the branches came from the same plane representing the half- k . To address this, a mapping procedure is created (Kupfer et al., 1987), where pinch points are discovered by mapping selected contour lines from the $(k_r - k_i)$ -plane into the $(\omega_r - \omega_i)$ -plane. When these lines are deformed, a branch point termed a cusp point appears in the ω -plane. Simultaneously, a pinch point emerges in the $(k_r - k_i)$ -plane. Additional distortions of contour lines after the establishment of the pinch point violate causality, and these deformations are halted. The following procedure can be used to determine whether or not the cusp point was formed by the k -branches created from two various halves of the $(k_r - k_i)$ -plane. As stated by (Kupfer et al., 1987), one can determine whether or not a pinch point exists at a cusp point by drawing a straight beam (parallel to the $Re(\omega_r)$ -axis) starting from the cusp point and finishing with the first contour image (for $k_i = 0$) and counting the intersections at which the beam intersects this image. If the number of the intersections is odd, then we are sure that the cusp point was formed by two various k -branches originating from two separate half of the $(k_r - k_i)$ -plane, and it is known as a pinch point.

8.1. Discovering the cusp point

(Kupfer et al., 1987) are shown that a $D(\omega, k) = 0$ dispersion relation may identify absolute instability from mapping the complex-frequency plane to the wavenumber plane. However, for a large number of physical techniques, the dispersion relation is used as a polynomial in ω rather than a transcendental in k . Solving for ω given a k is easier than solving for k given a ω . Because it is simpler to map from the $(k_r - k_i)$ -plane to the frequency plane than it is to solve transcendental equations (i.e. we can determine stability characteristics without having to solve them). The image of the region in the $(k_r - k_i)$ -plane is bounded on one side by the first contour created by mapping the complex wavenumber plane’s real line. Numerous contour lines exist throughout the range of unstable wavenumbers. If the contour lines are mapped into the $(\omega_r - \omega_i)$ -plane, each contour line

terminates in this specific area and leaves its image. A cusp point may be formed by constant parallel beams $Im(k) < 0$ mapped on the $(\omega_r - \omega_i)$ -plane. Assuming that a cusp point can be identified, it will correspond to the complex frequency plane value ω_0 in the $(\omega_r - \omega_i)$ -plane. This point is generated in the complex wavenumber plane by an associated value of $k = k_0$. We have $\partial D(\omega_0, k_0)/\partial k = 0$ and $D(\omega_0, k_0) = 0$ by definition. Pinch point is identified when ω_0 and k_0 are such that $\partial^2 D(\omega_0, k_0)/\partial k^2 \neq 0$. Thus, $\omega = \omega_0$ denotes the cusp point's position in the $(\omega_r - \omega_i)$ -plane, whereas $k(\omega_0)$ denotes the saddle point's position in the k -plane corresponding to the cusp point ω_0 . One can conclude that the relationship, $(k - k_0)^2 \sim \omega - \omega_0$, is a basic characteristic of forming the branching point (the cusp point) in the complex ω -plane, depending on whether the pinch point in the $(k_r - k_i)$ -plane is a saddle point or not. To search the cusp point, search the plane of k through k_r -contour lines with different $k_i < 0$ values and plot the contour lines images in the complex ω -plane. When the contour lines are close to the singularity, these images of the contour lines form a cusp. A contour line with the exact cusp point (ω_0) will appear on one of these contour lines. Once the cusp point is determined, the sign of ω_0 can be used to identify the type of instability (convective or absolute). The flow of the liquid jet is absolutely unstable if $\omega_{0r} > 0$, and convectively unstable if $\omega_{0r} < 0$; otherwise, the flow is stable (see Li et al., 2019).

Cusp map method does not depend on any mathematical formulae to determine where a cusp should be placed. Rather than that, we consider mappings of our k contours onto the frequency plane (varying real part, fixed imaginary part). This results in a curve that frequently loops back on itself. Therefore following the idea of the cusp map method by looking at line mappings with $Im(k) = k_i$ (constant) in the $(k_r - k_i)$ -plane on the $(\omega_r - \omega_i)$ -plane is referred to as the cusp curve, which is a set of points. Applying this method, if $k_i = 0$ and keep changing k_r -values yields the image of 1st contour of the dispersion relation, which corresponds to the largest growth rate of the temporal instability, as depicted in Fig. 4 when $Pe = 10$ (the blue one). When k_i values are reduced to negative values, we obtain the corresponding images of the dispersion relation, (32), in the $(\omega_r - \omega_i)$ -plane as depicted in Fig. 12. If $k_i = -0.2$, we observe that the cusp point appears at $\omega_0 = 0.068 - 0.81i$, which corresponds to the k_0 (the saddle point) in the $(k_r - k_i)$ -plane. This is called a pinch point because when we draw a straight beam parallel to the $Re(\omega)$ -axis from it to the image of the 1st k_r -contour line (for $k_i = 0$) in the $(\omega_r - \omega_i)$ -plane, there is only a point of intersection (odd number) (see (Patne and Shankar, 2017, Camporeale et al., 2017)). In Fig. 12, the flow is absolutely unstable due to the fact that $\omega_{0r} > 0$.

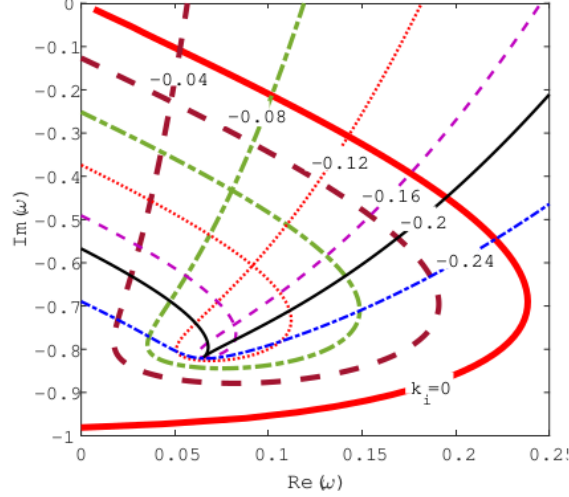


Figure 12: Graph illustrating the k_r -contour for various k_i values in the $(\omega_r - \omega_i)$ plane. The black line represents the cusp curve (when $k_i = -0.2$), contains the cusp point, whereas the red thick line represents the 1st k_r -contour (when $k_i = 0$). Where $F = 4$, $De = 10$, $\mu_H = 0.2$, $Pe = 10$, $Bi = 0.2$, $\sigma_H = 0.1$, $Re = 800$ and $We = 2$ at $z = 0$.

8.2. Discovering the saddle point

We utilize the saddle point method, as described in (Bassi, 2011) and (Balestra et al., 2015), to find the dispersion relation solutions, i.e. $D(\omega_0, k_0) = 0$, where $\frac{\partial D(\omega_0, k_0)}{\partial k^2} \neq 0$ and $D(\omega_0, k_0) = \frac{\partial D(\omega_0, k_0)}{\partial k} = 0$. To investigate how changing dimensionless parameters behave, we chose a reference state where $We = 2$, $F = 4$, $Pe = 10$, $Bi = 0.2$, $\mu_H = 0.2$, $\sigma_H = 0.1$, $Re = 800$, and $De = 10$ at $z = 0$. Also, the dispersion relation, (32), is solved spatially to find the saddle point using the numerical Newton-Raphson method in the $(k_r - k_i)$ -plane. In general, two separate branches of spatial curves exist for $D(\omega, k) = 0$, each branch is composed of a pair of points on either side of the saddle point. Examining ω_i contour lines by reducing ω_r values gradually to zero, and using the Newton-Raphson method to resolve the dispersion relation for k reveals these points. A saddle point is created when the two ω_i -contour lines come close to meeting each other at the point where $k = k_0$ and when ω_r values are reduced from positive little values to zero.

It is crucial to keep in mind that the cusp point in the $(\omega_r - \omega_i)$ -plane corresponds to the pinch point in the $(k_r - k_i)$ -plane, which must be taken into consideration when determining the saddle point. This is the case due to the fact that the

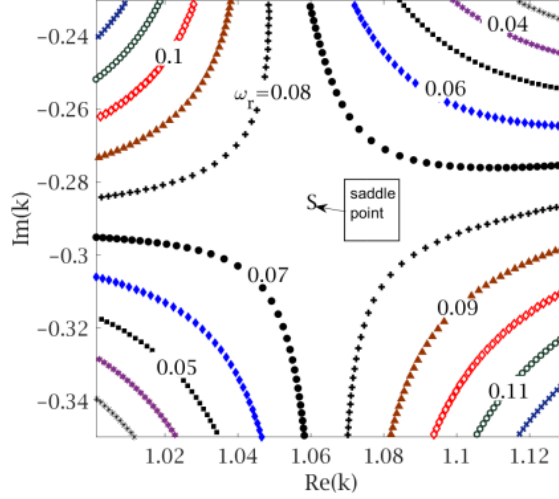


Figure 13: Graph illustrating the saddle point, which is located in the complex k -plane at $k_0 = 1.062 - 0.288i$, between 2 spatial branches of $Im(\omega)$ contour (when $Re(\omega) = 0.07$ and $\omega_r = 0.08$ respectively). Where $De = 10$, $Pe = 10$, $Bi = 0.2$, $F = 4$, $\mu_H = 0.2$, $\sigma_H = 0.1$, $Re = 800$ and $We = 2$ at $z = 0$.

group speed is equal to 0 not only at the pinch point but also at the confluence of the two k -branches. This is the case irrespective of whether the branches formed from different halves of the same k -plane or from the same half of the same k -plane. To guarantee that the first-order saddle point is correctly located, we must utilize ω_i -contour for numerous positive little values of ω_r on the complex k -plane near the real part of the cusp point (ω_{0r}). After this, we numerically solve the dispersion relation for k by applying the Newton-Raphson method. A reader of the method above can find that the saddle point is found at $k_0 = 1.069 - 0.281i$, between 2 spatial curves ($\omega_r = 0.07$ and $\omega_r = 0.08$), as depicted in Fig. 13. We have verified that ω_0 and k_0 satisfy the requirements of the pinch point conditions (i.e. $\partial^2 D(\omega_0, k_0) / \partial k^2 \neq 0$, $\partial D(\omega_0, k_0) / \partial k = 0$ and $D(\omega_0, k_0) = 0$). (See Briggs, 1964, Vesipa et al., 2014)

8.3. Discovering the CAIB

In order to locate the CAIB (convective-absolute instability boundary), we must monitor the cusp point as the Weber number is increased and all other dimensionless parameters are held fixed. We then find ω values at the cusp point using the Newton-Raphson method. This procedure is repeated until the Weber

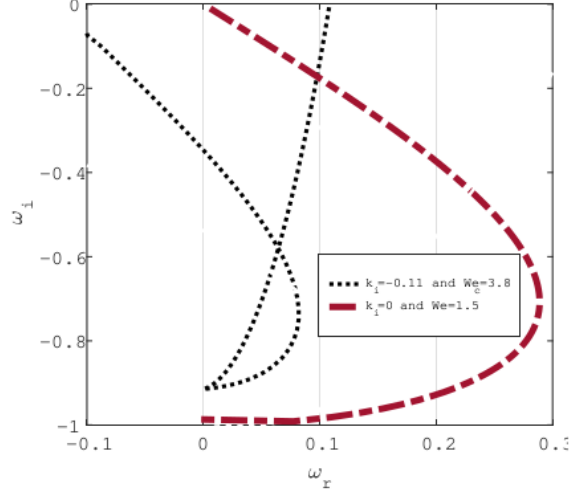


Figure 14: Graph of cusp point movement in the complex ω plane. When $We = 1.5$, the thick red dashed line is the first contour line (for $k_i = 0$); while the blue line is the cusp curve (for $k_i = -0.11$), which indicates the transition from (AI) to (CI), when $We = We_c = 3.8$. Where $De = 10$, $F = 4$, $\mu_H = 0.2$, $\sigma_H = 0.1$, $Pe = 10$, $Bi = 0.2$, $Re = 800$ and $We = 2$ at $z = 0$.

number reach a critical value (that is, when the sign of ω_r changes from negative to positive), the critical value of $We = We_c$ at which the transition occurs from absolutely unstable to convectively unstable, i.e. $\omega_{0r} = 0$, depicted in Fig. 14. In this case, the critical value of We (i.e., We_c) will be used to identify the convective/absolute instability boundary (CAIB), which will be the boundary between the convective and absolute regions (see Mohamed et al. 2015, Li et al., 2011). The same procedure is followed for various values of Re in the $(Re - We)$ -plane, as depicted in Fig. 15, and in the $(We - De)$ -plane, as depicted in Fig. 16, where We_c denotes the location of the CAIB. Finally, in Fig. 17, the CAIB is identified by We_c values, with different values of Bi , in the $(We - Bi)$ -plane using the same process above.

Also, in Fig. 15, we observe that when the viscosity reduces (by increasing Re values), the CAIB increases (i.e. an increase in We_c values), where the CAIB increases abruptly in the range $(500 > Re > 0)$, and then rises progressively when $Re > 500$, indicating a delay in the transition from absolute to convective instability. According to its qualitative behavior, the CAIB is similar to that observed in (López-Herrera et al., 2010, Lin and Lian, 1989, 1993). Additionally, we observe that the inclusion of heating decreases We_c values for various values of Re . In

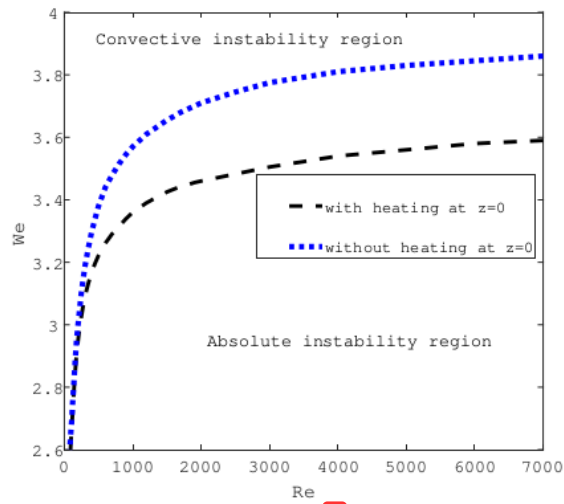


Figure 15: On the $Re-We$ plane, a graph depicting the convective/absolute instability boundary (CAIB) emerges at $\omega_r = 0$. Where $De = 10$, $F = 4$, $Pe = 10$, $Bi = 0.2$, $\mu_H = 0.2$, $\sigma_H = 0.1$ at $z = 0$.

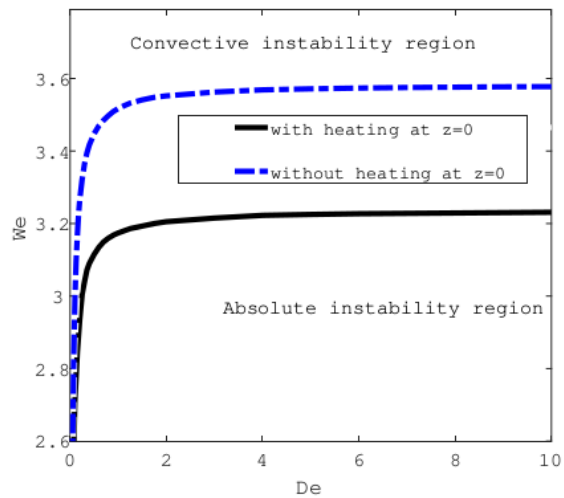


Figure 16: On the $De-We$ plane, a graph depicting the convective/absolute instability boundary (CAIB) emerges at $\omega_r = 0$. Where $Re = 800$, $F = 4$, $Pe = 10$, $Bi = 0.2$, $\mu_H = 0.2$, $\sigma_H = 0.1$ at $z = 0$.

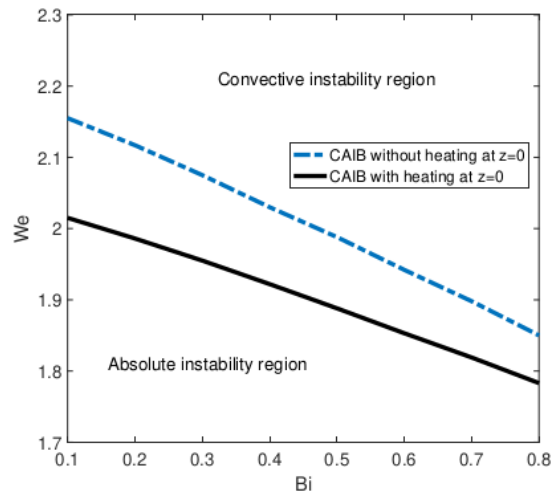


Figure 17: On the $Bi-We$ plane, a graph depicting the convective/absolute instability boundary (CAIB) emerges at $\omega_r = 0$. Where $Re = 800$, $Pe = 10$, $De = 10$, $F = 4$, $\mu_H = 0.2$, $\sigma_H = 0.1$ at $z = 0$.

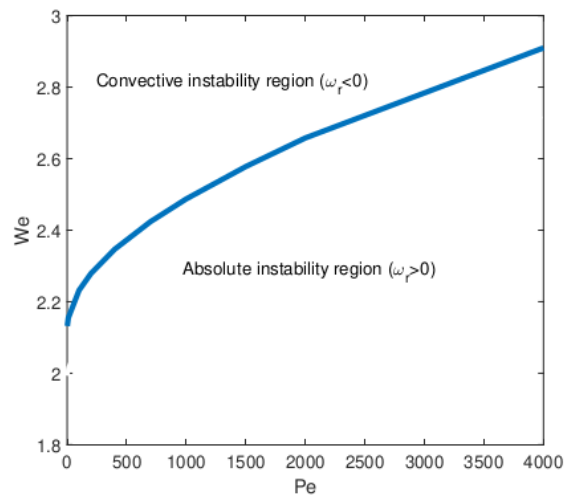


Figure 18: On the $Pe-We$ plane, a graph depicting the convective/absolute instability boundary (CAIB) emerges at $\omega_r = 0$. Where $Re = 800$, $Bi = 0.2$, $De = 10$, $F = 4$, $\mu_H = 0.2$, $\sigma_H = 0.1$ at $z = 0$.

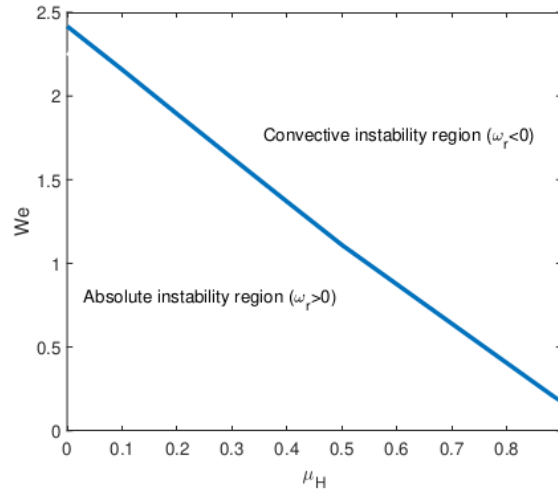


Figure 19: On the μ_H - We plane, a graph depicting the convective/absolute instability boundary (CAIB) emerges at $\omega_r = 0$. Where $Re = 800$, $Bi = 0.2$, $Pe = 10$, $De = 10$, $F = 4$, $\sigma_H = 0.1$ at $z = 0$.

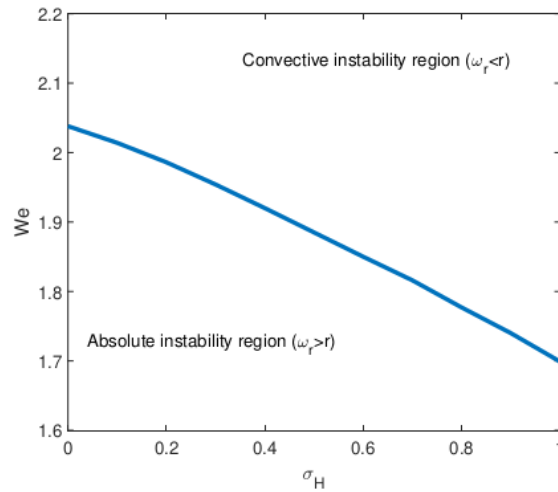


Figure 20: On the σ_H - We plane, a graph depicting the convective/absolute instability boundary (CAIB) emerges at $\omega_r = 0$. Where $Re = 800$, $Bi = 0.2$, $Pe = 10$, $De = 10$, $F = 4$, $\mu_H = 0.2$ at $z = 0$.

addition, we can see from this figure that the inclusion of heating has resulted in a smaller region of absolute instability being observed. In a similar way to gravitational forces, the Marangoni-induced flow, which works in the direction of gravity, acts in the opposite direction of wave propagation, preventing it from propagating upstream. Fig. 16 shows a sharp rise in CAIB ($1 > De > 0$) and then asymptotes, which shows that the highest value of We_c is 3.6 without heating, while the largest value of We_c is 3.22 with heating. In Fig. 17, the CAIB (i.e. the critical Weber number) decreases as the Biot number rises, implying that the flow is absolutely unstable when both the Weber and Biot numbers are simultaneously decreased. Additionally, we observe that the maximum value of We_c decreases with heating. Moreover, we plot the CAIB on the $Pe - We$ plane as depicted in Fig. 18. We note, from this figure, that the critical Weber number (We_c) increases as the Peclet number increases. While the critical Weber number is decreased by increasing the value of μ_H as depicted in Fig. 19. Also, increasing the value of σ_H leads to a decrease in We_c as illustrated in Fig. 20.

9. conclusion

This paper has looked into the (CI) and (AI) of a viscoelastic liquid jet that has fallen under the influence of gravity. We have used the UCM model and obtained steady basic flow solutions using an asymptotic approach. Perturbations to these basic flow solutions result in the formation of a dispersion relation, which has numerically solved. A mapping approach created by (Kupfer et al., 1987) has been used to find the cusp and pinch points for absolute instability. Also, the CAIB has been identified for different parametric regimes. In particular, we have examined the influence of heat transfer on the (CI) and (AI) of viscoelastic liquid jets. We have found that dripping-to-jetting transitions occur at lower values of the critical Weber number when the heat transfer to the interface of the viscoelastic liquid jet is taken into account. Furthermore, for lower values of the Weber number, the jet is absolutely unstable for fixed Reynolds, Deborah, and Biot numbers. In applications in which absolute instability is desired (as in spray formation), the Weber number must be decreased. In conclusion, the presence of the thermocapillary effect always causes breakup to be delayed, resulting in longer jets (that is, thermocapillary has a stabilizing influence on jet disintegration). The thermocapillary effect also decreases the critical Weber numbers (We_c) related with the parameters Re , De and Bi .

The work's results will be used in industrial processes that use viscoelastic liquid jets. These comprise recent advancements in needle-free injections, where

new research demonstrates the critical role of jet coherence in needle-free injection success (see Moradiafrapoli and Marston, 2017). Additionally, this paper is pertinent to recent advancements in nanofiber production, where the use of viscoelastic polymer solutions is crucial for liquid jet stability (see Gadkari, 2017). Finally, for jets with very tiny diameters (in nanofiber manufacturing, liquid jets have average diameters of roughly 10 μm) and at a high velocity, the surrounding medium will significantly impact jet dynamics and instability. These impacts will be investigated in a future article.

Acknowledgments

13 A. Alhushaybari would like to thank Taif University for the financial support. This work is supported by the Deanship of Scientific Research; Taif University; Saudi Arabia [1-442-66].

Appendix A.

The continuity equation (3) changes when dimensionless scalings (13) are used, and becomes

$$\frac{1}{\varepsilon} \left(\frac{\partial v_r}{\partial r} + \frac{v_r}{r} \right) + \frac{\partial v_z}{\partial z} = 0. \quad (\text{A.1})$$

Also, using the dimensionless scalings (13), the Navier-Stokes equation (4) is written in two components (the radial and axial components), which are respectively

$$\begin{aligned} \varepsilon \left(\frac{\partial v_r}{\partial t} + v_z \frac{\partial v_r}{\partial z} \right) + v_r \frac{\partial v_r}{\partial r} + \frac{\partial p}{\partial r} = \frac{1 + \mu_H(H-1)}{Re} \left[\frac{\partial^2 v_r}{\partial r^2} + \frac{1}{r} \frac{\partial v_r}{\partial r} - \frac{v_r}{r^2} + \varepsilon^2 \frac{\partial^2 v_r}{\partial z^2} \right] \\ + \frac{\varepsilon}{Re} \left(\frac{\partial T_{rr}}{\partial r} + \frac{T_{rr}}{r} + \varepsilon \frac{\partial T_{zr}}{\partial z} \right) + \frac{2}{Re} \frac{\partial v_r}{\partial r} \frac{\partial \mu}{\partial r} + \frac{\varepsilon}{Re} \frac{\partial \mu}{\partial z} \left(\frac{\partial v_z}{\partial r} + \varepsilon \frac{\partial v_r}{\partial z} \right), \quad (\text{A.2}) \end{aligned}$$

$$\begin{aligned} \varepsilon \left(\frac{\partial v_z}{\partial t} + v_z \frac{\partial v_z}{\partial z} \right) + v_r \frac{\partial v_z}{\partial r} = -\varepsilon \frac{\partial p}{\partial z} + \frac{1 + \mu_H(H-1)}{Re} \left(\frac{\partial^2 v_z}{\partial r^2} + \frac{1}{r} \frac{\partial v_z}{\partial r} + \varepsilon^2 \frac{\partial^2 v_z}{\partial z^2} \right) \\ + \frac{\varepsilon}{Re} \left(\varepsilon \frac{\partial T_{zz}}{\partial z} + \frac{T_{rz}}{r} + \frac{\partial T_{rz}}{\partial r} \right) + \frac{\partial \mu}{\partial z} \frac{2\varepsilon^2}{Re} \frac{\partial v_z}{\partial z} + \frac{1}{Re} \frac{\partial \mu}{\partial r} \left(\frac{\partial v_z}{\partial r} + \varepsilon \frac{\partial v_r}{\partial z} \right) + \frac{1}{F^2}. \quad (\text{A.3}) \end{aligned}$$

Also, using the dimensionless scalings (13), the extra stress tensor, (1), can be written in three components are

$$\begin{aligned} \varepsilon \frac{\partial T_{rz}}{\partial t} + v_r \frac{\partial T_{rz}}{\partial r} + \varepsilon v_z \frac{\partial T_{rz}}{\partial z} - T_{rz} \left(\frac{\partial v_r}{\partial r} + \varepsilon \frac{\partial v_z}{\partial z} \right) - \varepsilon T_{zz} \frac{\partial v_r}{\partial z} - T_{rr} \frac{\partial v_z}{\partial r} \\ = \frac{1 + \mu_H(H-1)}{De} \left(\varepsilon \frac{\partial v_r}{\partial z} + \frac{\partial v_z}{\partial r} - \varepsilon T_{rz} \right), \quad (\text{A.4}) \end{aligned}$$

$$\begin{aligned} \varepsilon \left(\frac{\partial T_{zz}}{\partial t} + v_z \frac{\partial T_{zz}}{\partial z} \right) + v_r \frac{\partial T_{zz}}{\partial r} - 2T_{rz} \frac{\partial v_z}{\partial r} - 2\varepsilon T_{zz} \frac{\partial v_z}{\partial z} \\ = \frac{1}{De} \left(2(1 + \mu_H(H-1)) \varepsilon \frac{\partial v_z}{\partial z} - \varepsilon T_{zz} \right), \quad (\text{A.5}) \end{aligned}$$

$$\begin{aligned} \varepsilon \left(\frac{\partial T_{rr}}{\partial t} + v_z \frac{\partial T_{rr}}{\partial z} \right) + v_r \frac{\partial T_{rr}}{\partial r} - 2T_{rr} \frac{\partial v_r}{\partial r} - 2\varepsilon T_{rz} \frac{\partial v_r}{\partial z} \\ = \frac{1}{De} \left(2(1 + \mu_H(H-1)) \frac{\partial v_r}{\partial r} - \varepsilon T_{rr} \right). \quad (\text{A.6}) \end{aligned}$$

The energy equation, (8), using the dimensionless scalings (13), becomes

$$\varepsilon \frac{\partial H}{\partial t} + v_r \frac{\partial H}{\partial r} + \varepsilon v_z \frac{\partial H}{\partial z} = \frac{1}{\varepsilon Pe} \left(\frac{\partial^2 H}{\partial r^2} + \frac{1}{r} \frac{\partial H}{\partial r} + \varepsilon^2 \frac{\partial^2 H}{\partial z^2} \right), \quad (\text{A.7})$$

The normal boundary condition, (9), using the dimensionless scalings (13), becomes

$$\begin{aligned} p - \frac{1}{ReE_\varepsilon^2} \left(2(1 + \mu_H(H-1)) \frac{\partial v_r}{\partial r} + \varepsilon T_{rr} \right) + \frac{2\varepsilon}{ReE_\varepsilon^2} \left(\frac{\partial \zeta}{\partial z} \right) \left[(1 + \mu_H(H-1)) \times \right. \\ \left. \left(\varepsilon \frac{\partial v_r}{\partial z} + \frac{\partial v_z}{\partial r} \right) + \varepsilon T_{rz} \right] - \frac{\varepsilon^3}{ReE_\varepsilon^2} \left(\frac{\partial \zeta}{\partial z} \right)^2 \left(2(1 + \mu_H(H-1)) \frac{\partial v_z}{\partial z} + T_{zz} \right) = \\ \frac{\sigma}{We} \left(\frac{1}{\zeta E_\varepsilon} - \frac{\varepsilon^2}{E_\varepsilon^3} \left(\frac{\partial^2 \zeta}{\partial z^2} \right) \right) \text{ at } r = \zeta_0, \quad (\text{A.8}) \end{aligned}$$

16 where $E_\varepsilon = \sqrt{1 + \varepsilon^2 \left(\frac{\partial \zeta}{\partial z} \right)^2}$.

The tangential boundary condition, (10), using the dimensionless scalings (13), becomes

$$\begin{aligned} \frac{2\varepsilon(1+\mu_H(H-1))}{Re} \left(\frac{\partial \zeta}{\partial z} \right) \left(\frac{\partial v_r}{\partial r} - \varepsilon \frac{\partial v_z}{\partial z} \right) + \frac{1}{Re} \left(1 - \varepsilon^2 \left(\frac{\partial \zeta}{\partial z} \right)^2 \right) \times \\ \left((1+\mu_H(H-1)) \left(\varepsilon \frac{\partial v_r}{\partial z} + \frac{\partial v_z}{\partial r} \right) + \varepsilon T_{rz} \right) + \frac{\varepsilon^2}{Re} \left(\frac{\partial \zeta}{\partial z} \right) (T_{rr} - T_{zz}) = \\ \frac{E_\varepsilon}{We} \left(\varepsilon \frac{\partial \zeta}{\partial z} \frac{\partial \sigma}{\partial r} + \varepsilon \frac{\partial \sigma}{\partial z} \right) \text{ at } r = \zeta_0. \quad (\text{A.9}) \end{aligned}$$

The normal flux condition of heat, (11), using the dimensionless scalings (13), can be written as

$$\frac{\partial H}{\partial r} - \varepsilon^2 \frac{\partial \zeta}{\partial z} \frac{\partial H}{\partial z} = -\varepsilon Bi(H-1)E_\varepsilon \text{ at } r = \zeta_0. \quad (\text{A.10})$$

The kinematic boundary condition, (12), using the dimensionless scalings (13), becomes

$$\frac{1}{\varepsilon} v_r = \frac{\partial \zeta}{\partial t} + v_z \frac{\partial \zeta}{\partial z} \text{ at } r = \zeta_0. \quad (\text{A.11})$$

Appendix B.

To illustrate how the equation, (17), is derived, we replace the expressions, (15) and (16), into our non-dimensional equations, (A.1)-(A.11). After removing the tildes for simplicity, the continuity equation (A.1), to $O(1)$ and $O(\varepsilon)$, becomes respectively

$$v_{r0} = 0, \quad \text{and} \quad v_{r1} = -\frac{1}{2} \left(\frac{\partial v_{z0}}{\partial z} \right). \quad (\text{B.1})$$

The axial momentum equation (A.3), to $O(1)$ and $O(\varepsilon)$, becomes respectively

$$v_{z1} = 0, \quad (\text{B.2})$$

and

$$\begin{aligned} \frac{\partial v_{z0}}{\partial t} + v_{z0} \frac{\partial v_{z0}}{\partial z} = \frac{1+\mu_H(H_0-1)}{Re} \left(4v_{z2} + \frac{\partial^2 v_{z0}}{\partial z^2} \right) - \frac{\partial p_0}{\partial z} - \frac{2}{Re} \frac{\partial v_{z0}}{\partial z} \frac{\partial H_0}{\partial z} \\ + \frac{1}{Re} \frac{\partial T_{zz}^0}{\partial z} + \frac{1}{F^2}. \quad (\text{B.3}) \end{aligned}$$

The tangential boundary condition, (A.9), to $O(\varepsilon)$, becomes

$$O(\varepsilon) : v_{z2} = \frac{3}{2\zeta_0} \left(\frac{\partial \zeta_0}{\partial z} \right) \frac{\partial v_{z0}}{\partial z} + \frac{1}{4} \frac{\partial^2 v_{z0}}{\partial z^2} + \frac{1}{2[1 + \mu_H(H_0 - 1)]\zeta_0} \left[\frac{Re}{We} \frac{\partial \sigma_0}{\partial z} - \left(\frac{\partial \zeta_0}{\partial z} \right) (T_{rr}^0 - T_{zz}^0) \right]. \quad (\text{B.4})$$

The normal boundary condition, (A.8), to $O(1)$, becomes

$$p_0 = \frac{1}{Re} \left(T_{rr}^0 - [1 + \mu_H(H_0 - 1)] \frac{\partial v_{z0}}{\partial z} \right) + \frac{\sigma_0}{We\zeta_0}. \quad (\text{B.5})$$

By substituting equations (B.4 and B.5) into equation (B.3) give equation (17).

Appendix C.

Substituting (28) into our non-dimensional equations (in Appendix A), we obtain a system of ordinary differential equations that is

$$\bar{v}_z = \frac{-1}{ik} \left(\frac{\partial \bar{v}_r}{\partial r} + \frac{\bar{v}_r}{r} \right), \quad (\text{C.1})$$

$$(\omega + ikv_{z0})\bar{v}_r = \frac{1 + \mu_H(H_0 - 1)}{Re} \left(\frac{\partial^2 \bar{v}_r}{\partial r^2} + \frac{1}{r} \frac{\partial \bar{v}_r}{\partial r} - \frac{\bar{v}_r}{r^2} - k^2 \bar{v}_r \right) - \frac{\partial \bar{p}}{\partial r} + \frac{1}{Re} \left(\frac{\partial \bar{T}_{rr}}{\partial r} + \frac{\bar{T}_{rr}}{r} \right), \quad (\text{C.2})$$

$$(\omega + ikv_{z0})\bar{v}_z = \frac{1 + \mu_H(H_0 - 1)}{Re} \left(\frac{\partial^2 \bar{v}_z}{\partial r^2} + \frac{1}{r} \frac{\partial \bar{v}_z}{\partial r} - k^2 \bar{v}_z \right) - ik\bar{p} + \frac{1}{Re} (ik\bar{T}_{zz}), \quad (\text{C.3})$$

$$\bar{T}_{zz} = \frac{2ik}{(\omega + ikv_{z0})} \left(\frac{1 + \mu_H(H_0 - 1)}{De} + T_{zz}^0 \right) \bar{v}_z, \quad (\text{C.4})$$

$$\bar{T}_{rr} = \frac{2}{(\omega + ikv_{z0})} \left(\frac{1 + \mu_H(H_0 - 1)}{De} + T_{rr}^0 \right) \frac{\partial \bar{v}_r}{\partial r}, \quad (\text{C.5})$$

$$(\omega + ikz_0)\bar{H} = \frac{\partial^2 \bar{H}}{\partial r^2} + \frac{1}{r} \frac{\partial \bar{H}}{\partial r} - k^2 \bar{H}, \quad (\text{C.6})$$

$$\bar{p} = \frac{1}{Re} \left(\bar{T}_{rr} + 2[1 + \mu_H(H_0 - 1)] \frac{\partial \bar{v}_r}{\partial r} \right) + \frac{\sigma_0}{We} \left(k^2 - \frac{1}{\zeta_0^2} \right) \bar{\zeta} \text{ at } r = \zeta_0, \quad (\text{C.7})$$

$$[1 + \mu_H(H_0 - 1)] \left(ik\bar{v}_r + \frac{\partial \bar{v}_z}{\partial r} \right) + ik\bar{\zeta} (T_{rr}^0 - T_{zz}^0) = \frac{ikRe}{We} \bar{\sigma} \text{ at } r = \zeta_0, \quad (\text{C.8})$$

$$\frac{\partial \bar{H}}{\partial r} + ik(H_0 - 1)Bi\bar{\zeta} = 0 \text{ at } r = \zeta_0, \quad (\text{C.9})$$

$$\bar{\zeta} = \frac{\bar{v}_r}{(\omega + ikv_{z0})} \text{ at } r = \zeta_0. \quad (\text{C.10})$$

References

- A. Alhushaybari and J. Uddin. Convective and absolute instability of viscoelastic liquid jets in the presence of gravity. *Physics of Fluids*, 31(4):044106, 2019.
- J. N. Anno. The mechanics of liquid jets. *Lexington, Mass., DC Heath and Co., 1977. 118 p.*, 1977.
- J. Atencia and D. J. Beebe. Controlled microfluidic interfaces. *Nature*, 437(7059): 648, 2004.
- G. Balestra, M. Gloor, and L. Kleiser. Absolute and convective instabilities of heated coaxial jet flow. *Physics of Fluids*, 27(5):054101, 2015.
- R. Bassi. *Absolute instability in curved liquid jets*. PhD thesis, University of Birmingham, 2011.
- H. F. Bauer. Free liquid surface response induced by fluctuations of thermal marangoni convection. *AIAA journal*, 22(3):421–428, 1984.
- R. B. Bird, R. C. Armstrong, O. Hassager, and C. F. Curtiss. *Dynamics of polymeric liquids*, volume 1. Wiley New York, 1977.
- R. B. Bird, R. C. Armstrong, and O. Hassager. *Dynamics of polymeric liquids*. vol. 1: Fluid mechanics. 1987.

- R. J. Briggs. Electron-stream interaction with plasmas mit press. *Monograph MIT, Cambridge USA*, (29), 1964.
- D. Busker, A. Lamers, and J. Nieuwenhuizen. The non-linear break-up of an inviscid liquid jet using the spatial-instability method. *Chemical engineering science*, 44(2):377–386, 1989.
- C. Camporeale, R. Vesipa, and L. Ridolfi. Convective-absolute nature of ripple instabilities on ice and icicles. *Physical Review Fluids*, 2(5):053904, 2017.
- J. M. Chwalek, D. P. Trauernicht, C. N. Delametter, R. Sharma, D. L. Jeanmaire, C. N. Anagnostopoulos, G. A. Hawkins, B. Ambravaneswaran, J. C. Panditaratne, and O. A. Basaran. A new method for deflecting liquid microjets. *Physics of Fluids*, 14(6):L37–L40, 2002.
- C. Clasen, J. Eggers, M. A. Fontelos, J. Li, and G. H. McKinley. The beads-on-string structure of viscoelastic threads. *Journal of Fluid Mechanics*, 556: 283–308, 2006.
- P. G. Drazin and W. H. Reid. *Hydrodynamic stability*, 1981.
- Z. Du, X. Yu, and Y. Han. Inkjet printing of viscoelastic polymer inks. *Chinese Chemical Letters*, 29(3):399–404, 2018.
- J. Eggers. Nonlinear dynamics and breakup of free-surface flows. *Reviews of modern physics*, 69(3):865, 1997.
- J. Eggers and E. Villermaux. Physics of liquid jets. *Reports on progress in physics*, 71(3):036601, 2008.
- R. Faidley and R. Panton. Measurement of liquid jet instability induced by surface tension variations. *Experimental Thermal and Fluid Science*, 3(4):383–387, 1990.
- E. Furlani. Thermal modulation and instability of newtonian liquid microjets. In *2005 NSTI Nanotechnology Conference and Trade Show—NSTI Nanotech 2005 Technical Proceedings*, pages 668–671, 2005.
- S. Gadkari. Influence of polymer relaxation time on the electrospinning process: Numerical investigation. *Polymers*, 9(10):501, 2017.

- J. B. Keller, S. Rubinow, and Y. Tu. Spatial instability of a jet. *The physics of fluids*, 16(12):2052–2055, 1973.
- K. Kupfer, A. Bers, and A. Ram. The cusp map in the complex-frequency plane for absolute instabilities. *The Physics of fluids*, 30(10):3075–3082, 1987.
- S. Leib and M. Goldstein. Convective and absolute instability of a viscous liquid jet. *The Physics of fluids*, 29(4):952–954, 1986a.
- S. Leib and M. Goldstein. The generation of capillary instabilities on a liquid jet. *Journal of fluid mechanics*, 168:479–500, 1986b.
- F. Li, A. M. Gañán-Calvo, and J. M. López-Herrera. Absolute-convective instability transition of low permittivity, low conductivity charged viscous liquid jets under axial electric fields. *Physics of Fluids*, 23(9):094108, 2011.
- F. Li, B.-F. Wang, Z.-H. Wan, J. Wu, and M. Zhang. Absolute and convective instabilities in electrohydrodynamic flow subjected to a poiseuille flow: a linear analysis. *Journal of Fluid Mechanics*, 862:816–844, 2019.
- S. Lin and Z. Lian. Absolute instability of a liquid jet in a gas. *Physics of Fluids A: Fluid Dynamics*, 1(3):490–493, 1989.
- S. Lin and Z. Lian. Absolute and convective instability of a viscous liquid jet surrounded by a viscous gas in a vertical pipe. *Physics of Fluids A: Fluid Dynamics*, 5(3):771–773, 1993.
- J. M. López-Herrera, A. M. Gañán-Calvo, and M. A. Herrada. Absolute to convective instability transition in charged liquid jets. *Physics of Fluids*, 22(6):062002, 2010.
- S. Manna, S. Kundu, and J. Misra. Theoretical analysis of torsional wave propagation in a heterogeneous aeolotropic stratum over a voigt-type viscoelastic half-space. *International Journal of Geomechanics*, 18(6):04018050, 2018.
- A. S. Mohamed, M. Herrada, A. Gañán-Calvo, and J. Montanero. Convective-to-absolute instability transition in a viscoelastic capillary jet subject to unrelaxed axial elastic tension. *Physical Review E*, 92(2):023006, 2015.
- M. Moradiafrapoli and J. Marston. High-speed video investigation of jet dynamics from narrow orifices for needle-free injection. *Chemical Engineering Research and Design*, 117:110–121, 2017.

- N. M. Nahas and R. L. Panton. Control of surface tension flows: instability of a liquid jet. 1990.
- R. Patne and V. Shankar. Absolute and convective instabilities in combined couette-poiseuille flow past a neo-hookean solid. *Physics of Fluids*, 29(12):124104, 2017.
- D. Pramanik and S. Manna. Dynamic behavior of material strength due to the effect of prestress, aeolotropy, non-homogeneity, irregularity, and porosity on the propagation of torsional waves. *Acta Mechanica*, 233(3):1125–1146, 2022.
- D. K. Sharma, M. Bachher, S. Manna, and N. Sarkar. Vibration analysis of functionally graded thermoelastic nonlocal sphere with dual-phase-lag effect. *Acta Mechanica*, 231(5):1765–1781, 2020.
- T. Si, F. Li, X.-Y. Yin, and X.-Z. Yin. Modes in flow focusing and instability of coaxial liquid–gas jets. *Journal of Fluid Mechanics*, 629:1–23, 2009.
- F. Suñol and R. González-Cinca. Liquid jet breakup and subsequent droplet dynamics under normal gravity and in microgravity conditions. *Physics of Fluids*, 27(7):077102, 2015.
- J. Uddin. *An investigation into methods to control breakup and droplet formation in single and compound liquid jets*. PhD thesis, Ph. D. thesis, University of Birmingham, Birmingham, UK, 2007.
- M. Verhoef, B. Van den Brule, and M. Hulsen. On the modelling of a pib/pb boger fluid in extensional flow. *Journal of non-newtonian fluid mechanics*, 80(2-3):155–182, 1999.
- R. Vesipa, C. Camporeale, L. Ridolfi, and J. M. Chomaz. On the convective-absolute nature of river bedform instabilities. *Physics of Fluids*, 26(12):124104, 2014.
- L. Xie, L.-j. Yang, L.-z. Qin, and Q.-f. Fu. Temporal instability of charged viscoelastic liquid jets under an axial electric field. *European Journal of Mechanics-B/Fluids*, 66:60–70, 2017.
- J.-J. Xu and S. H. Davis. Instability of capillary jets with thermocapillarity. *Journal of Fluid Mechanics*, 161:1–25, 1985.

16%

SIMILARITY INDEX

PRIMARY SOURCES

1	research.birmingham.ac.uk Internet	658 words — 7%
2	aip.scitation.org Internet	307 words — 3%
3	pure-oai.bham.ac.uk Internet	163 words — 2%
4	repository.tudelft.nl Internet	35 words — < 1%
5	theses.bham.ac.uk Internet	33 words — < 1%
6	Abdullah Alsharif. "Spatial instability and break-up of viscoelastic Giesekus curved jets with surfactants", Fluid Dynamics Research, 2018 Crossref	22 words — < 1%
7	diposit.ub.edu Internet	20 words — < 1%
8	J. M. López-Herrera, P. Riesco-Chueca, A. M. Gañán-Calvo. "Linear stability analysis of axisymmetric perturbations in imperfectly conducting liquid jets", Physics of Fluids, 2005 Crossref	18 words — < 1%

9	academic.oup.com Internet	16 words — < 1%
10	Zhanjun Gao. "Instability of non-Newtonian jets with a surface tension gradient", <i>Journal of Physics A Mathematical and Theoretical</i> , 02/13/2009 Crossref	15 words — < 1%
11	Ramkarn Patne, V. Shankar. "Absolute and convective instabilities in combined Couette-Poiseuille flow past a neo-Hookean solid", <i>Physics of Fluids</i> , 2017 Crossref	14 words — < 1%
12	library.seg.org Internet	14 words — < 1%
13	www.mdpi.com Internet	13 words — < 1%
14	A Alhushaybari, J Uddin. "Convective and absolute instability of falling viscoelastic liquid jets surrounded by a gas", <i>IMA Journal of Applied Mathematics</i> , 2020 Crossref	12 words — < 1%
15	Alexander Pretty, Christopher Davies, Christian Thomas. "Onset of absolutely unstable behaviour in the Stokes layer: a Floquet approach to the Briggs method", <i>Journal of Fluid Mechanics</i> , 2021 Crossref	12 words — < 1%
16	core.ac.uk Internet	12 words — < 1%
17	tigerprints.clemson.edu Internet	12 words — < 1%

- 18 A. Alhushaybari, J. Uddin. "Convective and absolute instability of viscoelastic liquid jets in the presence of gravity", *Physics of Fluids*, 2019
Crossref 11 words — < 1%
-
- 19 EPHRAIM ELIAV UZI KALDOR YASUYUKI I. "The relativistic coupled-cluster method: transition energies of bismuth and eka-bismuth", *Molecular Physics*, 2010
Crossref 11 words — < 1%
-
- 20 M. Hamadiche, M. Gad-el-Hak. "Spatiotemporal Stability of Flow through Collapsible, Viscoelastic Tubes", *AIAA Journal*, 2004
Crossref 11 words — < 1%
-
- 21 api-depositonce.tu-berlin.de
Internet 11 words — < 1%
-
- 22 Fang Li, Alfonso M. Gañán-Calvo, José M. López-Herrera, Xie-Yuan Yin, Xie-Zhen Yin. "Absolute and convective instability of a charged viscoelastic liquid jet", *Journal of Non-Newtonian Fluid Mechanics*, 2013
Crossref 10 words — < 1%
-
- 23 Fang Li, Xie-Yuan Yin, Xie-Zhen Yin. "Transition from a beads-on-string to a spike structure in an electrified viscoelastic jet", *Physics of Fluids*, 2017
Crossref 10 words — < 1%
-
- 24 Yang, Li-Jun, Ming-Xi Tong, and Qing-Fei Fu. "Linear stability analysis of a three-dimensional viscoelastic liquid jet surrounded by a swirling air stream", *Journal of Non-Newtonian Fluid Mechanics*, 2013.
Crossref 10 words — < 1%
-
- 25 cs.swan.ac.uk
Internet 10 words — < 1%

26	pdffox.com Internet	10 words — < 1%
27	www.repository.cam.ac.uk Internet	10 words — < 1%
28	www.waset.org Internet	10 words — < 1%
29	yakari.polytechnique.fr Internet	10 words — < 1%

EXCLUDE QUOTES OFF

EXCLUDE BIBLIOGRAPHY ON

EXCLUDE SOURCES OFF

EXCLUDE MATCHES < 10 WORDS